



Natural Resources
Canada Ressources naturelles
Canada

**GEOLOGICAL SURVEY OF CANADA
OPEN FILE 8704**

**Detailed explanation of modelling absorption due to polar
cap absorption and shortwave fadeout**

R. A. D. Fiori

2020

Canada 



GEOLOGICAL SURVEY OF CANADA OPEN FILE 8704

Detailed explanation of modelling absorption due to polar cap absorption and shortwave fadeout

R. A. D. Fiori

Canadian Hazards Information Service, 2617 Anderson Road, Ottawa, Ontario K1A 0Y3

2020

© Her Majesty the Queen in Right of Canada, as represented by the Minister of Natural Resources, 2020

Information contained in this publication or product may be reproduced, in part or in whole, and by any means, for personal or public non-commercial purposes, without charge or further permission, unless otherwise specified.

You are asked to:

- exercise due diligence in ensuring the accuracy of the materials reproduced;
- indicate the complete title of the materials reproduced, and the name of the author organization; and
- indicate that the reproduction is a copy of an official work that is published by Natural Resources Canada (NRCan) and that the reproduction has not been produced in affiliation with, or with the endorsement of, NRCan.

Commercial reproduction and distribution is prohibited except with written permission from NRCan. For more information, contact NRCan at nrcan.copyrightdroitdauteur.rncan@canada.ca.

Permanent link: <https://doi.org/10.4095/321793>

This publication is available for free download through GEOSCAN (<https://geoscan.nrcan.gc.ca/>).

Recommended citation

Fiori, R. A. D., 2020. Detailed explanation of modelling absorption due to polar cap absorption and shortwave fadeout; Geological Survey of Canada, Open File 8704, 25 p. <https://doi.org/10.4095/321793>

Publications in this series have not been edited; they are released as submitted by the author.

1. List of Abbreviations

| | |
|--|----------|
| Canadian Space Weather Forecast Center | CSWFC |
| Coronal Mass Ejection | CME |
| Extreme Ultraviolet | EUV |
| Highest Affected Frequency | HAF |
| High Frequency | HF |
| Interactive Data Language | IDL |
| Magnetic Latitude | MLAT |
| Polar Cap Absorption | PCA |
| Quiet Day Curve | QDC |
| Natural Resources Canada | NRCan |
| relative ionospheric opacity meter | riometer |
| Root-Mean-Square Error | RMSE |
| Solar Proton Event | SPE |
| Singular Value Decomposition | SVD |
| Space Weather Prediction Center | SWPC |

2. Table of Contents

| | | |
|--------|---|----|
| 1. | List of Abbreviations | 2 |
| 2. | Table of Contents | 3 |
| 3. | Introduction | 4 |
| 4. | Modelling shortwave fadeout..... | 6 |
| 5. | Modelling polar cap absorption..... | 7 |
| 5.1. | Calculating Integral Proton Flux | 8 |
| 5.1.1. | Calculating Invariant Latitude..... | 9 |
| 5.1.2. | Calculating Equivalent K _p | 10 |
| 5.1.3. | Calculating the Vertical Cutoff Rigidity (E _c)..... | 11 |
| 5.1.4. | Calculating Integral Proton Flux..... | 12 |
| 6. | Input data and instrumentation | 13 |
| 6.1. | RiometerS..... | 13 |
| 6.2. | GOES satellite data..... | 15 |
| 6.3. | Magnetic Indices..... | 15 |
| 7. | Algorithm | 15 |
| 8. | Summary | 21 |
| 9. | References..... | 22 |

3. Introduction

Space weather impacts high frequency (HF) (3-30 MHz) radio communication systems causing a partial to complete signal loss which affects industries and organizations dependent on HF radio communication such as the military, Canadian coast guard, aviation, and shipping industries (i.e., Hunsucker, 1992; Pirjola et al., 2005; National Research Council, 2008; Cannon et al., 2013; Neal et al., 2013; MacAlester and Murtagh, 2014; Frissell et al., 2014; 2019). HF radio communication relies on the ionospheric propagation of radio signals. On the way to a ground-based receiver, radio signals travel through the D-region ionosphere, which has a relatively low electron density, and then turn toward the ground due to either refraction or reflection in the much more dense E and/or F region ionospheres. Spatial and temporal variations of the electron density distribution in the ionosphere can lead to significant changes in the parameters of radio signals received on the ground. One of the well-known effects is additional radiowave absorption in the D region due to enhanced ionization produced through photoionization by X-ray and extreme ultraviolet (EUV) radiation, or by the precipitation of energetic particles into the ionosphere (Browne et al., 1995; Hunsucker and Hargreaves, 2003).

Absorption occurs when energy from energetic particles is dispersed as heat due to collisions with other particles in the ionosphere and is therefore an altitude-dependent parameter affected by particle collision frequency and recombination rates. Absorption increases when the electron density is enhanced by increased ionization. The sun is a major source of increased ionization and therefore absorption. Photoionization reactions between energetic photons from the sun and neutral particles in the Earth's upper atmosphere cause ionization and the creation of the ionosphere. Photoionization is the main production mechanism for the D-region ionosphere, which typically disappears at night when the earth no longer faces the sun.

Several space weather phenomena cause ionospheric disturbances affecting HF radio communication (Hunsucker, 1992; Pirjola et al., 2005; National Research Council, 2008; Cannon et al., 2013; Neal et al., 2013; MacAlester and Murtagh, 2014). Of these, the most prominent lead to specific absorption phenomena: polar cap absorption, auroral absorption, and shortwave fadeout.

At high-latitudes, disruption to HF radio communication is primarily due to polar cap absorption. Energetic protons expelled by coronal mass ejections (CMEs) and accelerated to near relativistic speeds by the CME shock front (Gopalswamy, 2003), reach the Earth after a few hours penetrating deep into the high-latitude D-region ionosphere causing absorption across the polar cap. This is called polar cap absorption (PCA), and can extend across the high-latitude region reaching as far equatorward as 60-65° magnetic latitude, depending on the level of geomagnetic activity (i.e., Hargreaves et al., 1993; Kavanagh et al., 2004; Kouznetsov et al., 2014). PCA is a relatively long-lived phenomenon lasting on the order of days, and is more strongly felt in the sunlit ionosphere leading to day/night and seasonal cycles of absorption.

Solar particles expelled, for example, by CMEs or coronal holes, and the interplanetary magnetic field associated with them, interact with the Earth's magnetosphere causing geomagnetic disturbances, which results in increased electron precipitation and ionization in the auroral oval (i.e., Hargreaves, 2010). Auroral absorption is localized in regions on the nightside ionosphere lasting several hours.

Solar flares emit electromagnetic radiation across the electromagnetic spectrum, most notably in X-ray and EUV radiation. Electromagnetic radiation emitted from the sun travels at the speed of light and

reaches the Earth ~8 minutes later causing ionization in the ionosphere on the sunlit side of the Earth. The effect is most pronounced at the subsolar point becoming weaker toward the terminator (e.g., Schumer, 2009). D-region ionization by hard X-rays results in an increase of the electron density and D-region absorption lasting on the order of 0.5-2 hours (Davies, 1990; Hargreaves, 1992). For strong events, electron density in the D-region can become enhanced by a factor of ~10 (Davies, 1990). Absorption caused by solar X-ray flares can potentially lead to a fadeout of short wave signals or shortwave fadeout (SWF) and, for example, a loss of radio communication in affected regions.

Although each form of absorption has a different space weather driver, each potentially impacts HF radio communication in the affected region of the ionosphere. Understanding ionospheric absorption is therefore of critical importance to users dependent on HF radio communication.

Ionospheric absorption is monitored using a relative ionospheric opacity meter (riometer). Riometers are passive instruments measuring the intensity of cosmic radio noise from extra-terrestrial sources (i.e., stars and galaxies) to characterize ionospheric opacity (Browne et al., 1995; Davies, 1990; Little and Leinbach, 1959). In the simplest case, riometers employ a single, zenith-pointed radio antenna, and measure signal voltage that is proportional to the sky noise. Sky noise varies regularly during a sidereal day; this variation is described by a quiet day curve (QDC). Absorption, measured in dB, is defined as the deviation of the received voltage from the expected value (i.e. the QDC) and is given by (Browne et al., 1995)

$$A(\text{dB}) = 10 \log \left(\frac{P}{P'} \right), \quad (1)$$

where P is the measured noise power (i.e., the voltage measured by the riometer) and P' is the noise power that would have been received on a quiet day (i.e., the QDC voltage). Typically, a signal frequency of 30 MHz is used allowing riometers to resolve absorption to changes of ~0.1 dB (Davies, 1990). Because the QDC cannot be known precisely and can only be determined by fitting a curve to data collected over a long period of time, low absorption values are less reliable. For examples, Foppiano and Bradley (1984) and Kavanagh et al. (2004) suggest a lower limit of 0.2 dB for reliability.

Currently, the primary operational empirical absorption model in use for PCA and SWF is the D-region absorption prediction, or D-RAP, model, managed by NOAA's space weather prediction center (SWPC) (Sauer and Wilkinson, 2008). The D-RAP SWF model is based on Stonehocker (1970) with modifications described in Schumer (2009) and relies on data from the GOES solar X-ray flux monitor. To model PCA, D-RAP uses established relationships between absorption and integral proton flux, derived from the GOES satellite measurements of the >10 MeV solar proton flux. PCA relationships for the dayside and nightside are based on parameters derived by Sellers et al. (1977) and Sauer and Wilkinson (2008).

Recently, Rogers and Honary (2015) proposed improvements to the D-RAP modelling technique through the incorporation of measurement-derived absorption values into the modelling technique. Based on a data set comprised of 94 solar proton events (SPEs) they show that data-based optimization of coefficients used in the equations which form the basis of the D-RAP model improves the agreement between measurement-derived and modelled absorption by as much as 36%. They demonstrate the potential use of their optimized D-RAP modelling approach for the purpose of real-time absorption modelling. Additional improvements to modelling absorption in the dayside / nightside transition region are suggested in Rogers et al. (2016).

This report describes, in detail, modelling techniques employed by the Canadian Space Weather Forecast Center (CSWFC) on the basis of SWF modelling techniques employed by D-RAP and using modelling techniques discussed by both Sauer and Wilkinson (2008) and improvements adopted by Rogers and Honary (2015) and Rogers et al. (2016). The following sections describe data, theory, and the algorithm governing the current modelling algorithm.

4. Modelling shortwave fadeout

SWF modelling follows methodologies employed by D-RAP (<http://www.swpc.noaa.gov/content/global-d-region-absorption-prediction-documentation>) which is built on work by Stonehocker (1970) and reported in Schumer (2009) and Rogers and Honary (2015). Modelling the contribution of SWF to absorption need only be performed if the solar X-ray flux is sufficient enough to influence absorption. Following D-RAP, a threshold level of $1.0 \times 10^{-5} \text{ Wm}^2$ (M1.0) is adopted.

The highest affected frequency (HAF) for a zenith-pointed radio antenna is given by

$$HAF = \cos^{0.75} \chi (10 \log F + 65) \text{ MHz} \quad (2)$$

where F is the solar X-ray flux at 0.1-0.8 nm, measured in Wm^2 , and χ is the solar zenith angle. By definition, HAF is the frequency at which a signal having vertical incidence is expected to suffer a 1 dB loss.

Absorption at 30 MHz is determined from HAF through

$$A_x(\text{dB}) = 0.5 \left(\frac{HAF}{30 \text{ MHz}} \right)^{1.5} \quad (3)$$

where the factor of 0.5 accounts for 1-way propagation (as the signal is absorbed in the D-region). Note that an f^2 relationship is more commonly employed, for scaling riometer absorption. However, Sauer and Wilkinson (2008), which is the model employed by D-RAP cite a relationship of $f^{1.5}$ and Schumer (2009) show that a relationship of $f^{1.24}$ is more accurate.

The cosine dependence on χ introduces diurnal variation in the data and requires HAF, and therefore A_x , to be greatest at the subsolar point when the sun is directly overhead, and falls off to zero for $|\chi| = 90^\circ$. Hunsucker and Hargreaves (2003) report that the coefficient of 0.75, which is also reported by Sauer and Wilkinson (2008), varies from 0.7 to 1.0 in the literature. Davies (1990) report that the coefficient varies based on magnetic latitude with a value of 0.85 ± 0.15 at low latitudes, 0.75 ± 0.15 at mid-latitudes, and 0.2 in the auroral zone. They do not report the coefficient equatorward of the auroral zone. Schumer (2009) uses a value of 0.90. Although the exact value of the coefficient is in debate, it is important that the term be included to allow absorption to taper off from a maximum value at the subsolar point to a minimum value at the terminator. On the nightside ($|\chi| > 90^\circ$) HAF and A_x are set to 0 as ionization by X-ray and EUV radiation is strictly a dayside phenomena.

These expressions for absorption do not have a seasonal dependence outside what is inherent in the χ term which is insufficient to account for the seasonal variation commonly observed in absorption. The $\cos \chi$ dependence is reasonable during summer and equinox, but inadequate during the winter month when absorption is 2-3 times higher than in summer month (Davies, 1990; Hunsucker and Hargreaves, 2003). This so called winter anomaly is a mid-latitude phenomena attributed to stratospheric warming. Currently a seasonally dependent relationship is not available.

Findings in Stonehocker (1970) are based on the response of the average signal attenuation of a 5 MHz transmission signal to a solar X-ray flare. The derived relationship is based on data collected for 46 solar X-ray flares during the summer months at a New Mexico station located in the 10-14 local time range. The relationships are verified with an error of < 9% for frequencies in the 5-12 MHz range. Schumer (2009) reports increasing inaccuracy in the absorption scaled to higher frequencies, and demonstrates a gross underestimation of absorption at 30 MHz, which was a motivating factor in using the $f^{-1.5}$ dependence opposed to the more commonly used f^2 dependence. These uncertainties suggest additional work is required to improve the relationships described in this Section. However, for the time being they are applied to match the D-RAP model. Future work will involve the improvement of this theory based on data from Canadian riometers.

5. Modelling polar cap absorption

As with SWF, PCA is modelled from D-RAP. Improvements are made based on methodologies presented in Rogers and Honary (2015) and Rogers et al. (2016).

PCA is a wide-spread phenomenon spanning the entire high-latitude region poleward of $\sim 65^\circ$ MLAT on both the dayside and nightside. Absorption modelling based purely on riometer data is not practical due to the relatively sparse distribution of riometers over the impacted region. Modelling has therefore focused on relationships observed between the measured absorption and the influx of solar protons driving the absorption. There is a simple and well-known dependence between absorption (A) and the square root of the omnidirectional integral proton flux (J) above a threshold energy (E_o) (e.g., Sellers et al., 1977)

$$A = m[J(E > E_o)]^{1/2} \quad (4)$$

where A is in units of dB, and $J(E > E_o)$ is in $(\text{cm}^2 \text{ s sr})^{-1}$. The proportionality constant, m , has units of dB $(\text{cm}^2 \text{ s sr})^{1/2}$. Sellers et al. (1977) evaluated 30 MHz data for a riometer located in Thule, Greenland for a series of proton events and determined the value of the proportionality constant on both the dayside and the nightside. These values are reported in Table 1.

Table 1: Equation (4) parameters for the Thule riometer as determined by Sellers et al. (1977).

| | m [dB($\text{cm}^2 \text{ s sr}$) $^{1/2}$] | E_o [MeV] |
|------------------|---|----------------|
| Dayside | 0.115 | 5.2 |
| Nightside | 0.020 | 2.2 |

Using the relationship reported in equation (4), and the proportionality constants derived by Sellers et al. (1977), Sauer and Wilkinson (2008) define expressions for modelling PCA on the dayside (D), nightside (N) and twilight (T) as follows:

$$A = \begin{cases} A_D = m_D[J(E > 5.2 \text{ MeV})]^{1/2} & \varepsilon \geq 10^\circ \\ A_N = m_N[J(E > 2.2 \text{ MeV})]^{1/2} & \varepsilon \leq -10^\circ \\ A_T = A_D \frac{\varepsilon+10^\circ}{20^\circ} - A_N \frac{\varepsilon-10^\circ}{20^\circ} & -10^\circ < \varepsilon < 10^\circ \end{cases} \quad (5)$$

where ε represents the solar elevation angle, which is defined as the angular height of the sun measured from the horizontal (i.e., $\varepsilon=0^\circ$ at sunrise and sunset and $\varepsilon=90^\circ$ when directly overhead), and m_D and m_N are given in Table 1.

Rogers and Honary (2015) point out that data sets in *Sellers et al.* (1977) and *Sauer and Wilkinson* (2008) are limited, and suggest optimizing the model through consideration of additional parameters, such as the measured absorption. To spatially interpolate measurement-derived absorption from stations distributed across the high-latitude region, they suggest optimizing the choice of m_D and m_N from equation (5) used in the D-RAP approach by minimizing the root-mean-square error (RMSE) between measured and modelled data at measurement coordinates using linear regression. The measurement data set for a given instant in time (t) is increased by including measurements from all available stations over the 30-minute interval preceding t . For a single event, Rogers and Honary (2015) visually demonstrate that the optimized D-RAP approach notably improves the agreement between measurement-derived and modelled absorption. Rogers et al. (2016) further improved their approach by replacing the linear transition from A_D to A_N in the twilight zone (A_T) seen in equation (5) with a more gradual Gauss error-function transition. Improvements reported by Rogers and Honary (2015) and Rogers et al. (2016) are incorporated into the CSWFC absorption model.

Modelling absorption would seem rather straight forward based on the limited amount of theory provided above. Simply take the integral proton flux and insert it into equation (5), compare this to absorption derived from the riometer data, and minimize the difference between the measured and modelled values to determine the optimal fitting coefficients on the dayside and nightside. Complications arise in determining the integral proton flux.

5.1. CALCULATING INTEGRAL PROTON FLUX

In practice, expressions for dayside and nightside integral proton flux presented in equations (4) and (5) are replaced by $J(E > \text{MAX}([5.2, E_c]))$ and $J(E > \text{MAX}([2.2, E_c]))$, respectively, where E_c is the minimum cutoff energy required by an energetic particle to reach an altitude of 50 km for a specific latitude (i.e., vertical cutoff rigidity). The reasoning behind this is that only protons capable of reaching a given point (altitude and latitude) should be included (i.e., *Rodger et al.*, 2006; *Neal et al.*, 2013). Determining the integral proton flux therefore first requires knowledge of the vertical cutoff rigidity described by E_c .

Fortunately, E_c has been determined by *Smart et al.* (1999) who computed the proton cutoff energy as a function of invariant latitude for various levels of geomagnetic activity at 450 km altitude, see Figure 2. Here geomagnetic activity refers to an ‘equivalent K_p index’ which is described below. Unfortunately, *Smart et al.* (1999) only present a Figure describing these relationships and do not include a table of numbers. However, a table of values was obtained from Dr. Neil Rogers courtesy of a summer student (Ben Pennington) who meticulously read the values from the Figure in *Smart et al.* (1999), see Table 2.

From Figure 1 and Table 2, we see that the cutoff energy E_c is determined based on the invariant latitude of the coordinate of interest and the geomagnetic activity level as defined by either the K_p or Dst/SYM-H index using *Smart et al.* (1999). Calculation of invariant latitude at 50 km altitude (required by D-RAP) and the equivalent K_p index, using these values to interpolate E_c from Figure 2, and finally using E_c to interpolate the integral proton flux from measurements are included in the following sections.

Note that the calculations outlined below will need to be performed any time the input variables (K_p or equivalent K_p, and integral proton flux) change.

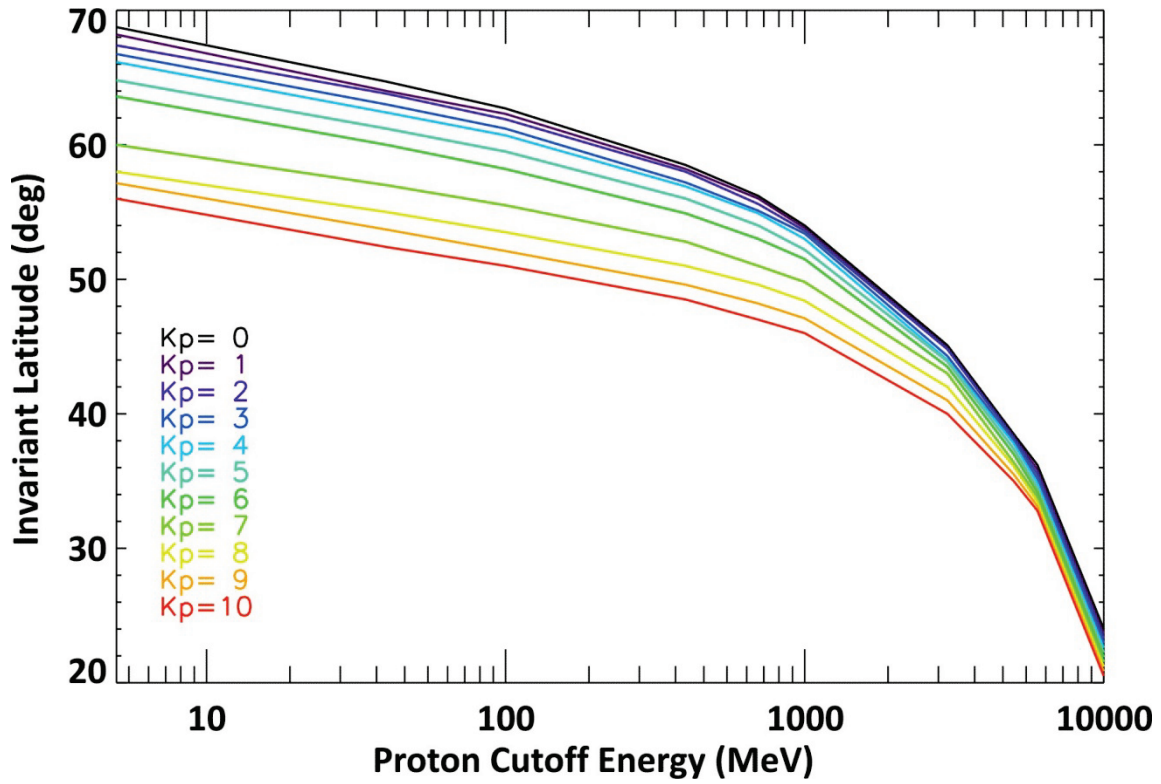


Figure 1: Proton cutoff energy as a function of invariant latitude and geomagnetic activity. Based on a similar diagram in Smart *et al.* (1999).

Table 2: Invariant latitude as a function of K_p' and cutoff energy as determined from Smart *et al.* (1999) at an altitude of 450 km.

| K_p' | 0 | E _c | | | | | | | | | | |
|--------|------|----------------|------|------|------|------|------|------|------|-------|-------|-------|
| | | 1 | 10 | 40 | 100 | 400 | 700 | 1000 | 3000 | 5000 | 6000 | 10000 |
| 1 | 71.9 | 67.4 | 64.7 | 62.7 | 58.5 | 56.2 | 54.0 | 45.1 | 38.5 | 36.2 | 24.0 | |
| 2 | 71.5 | 66.8 | 64.0 | 62.3 | 58.2 | 56.0 | 53.8 | 44.9 | 38.3 | 35.86 | 23.65 | |
| 3 | 70.2 | 66.2 | 63.8 | 61.9 | 58.0 | 55.6 | 53.6 | 44.8 | 38.2 | 35.52 | 23.3 | |
| 4 | 69.7 | 65.5 | 63.0 | 61.2 | 57.2 | 55.1 | 53.4 | 44.3 | 38.0 | 35.18 | 22.95 | |
| 5 | 69.1 | 64.9 | 62.4 | 60.7 | 56.9 | 54.9 | 53.0 | 44.0 | 37.8 | 34.84 | 22.6 | |
| 6 | 67.6 | 63.6 | 61.2 | 59.5 | 56.0 | 54.0 | 52.2 | 43.9 | 37.4 | 34.5 | 22.25 | |
| 7 | 66.4 | 62.4 | 60.0 | 58.2 | 54.9 | 53.0 | 51.5 | 43.5 | 37.0 | 34.16 | 21.9 | |
| 8 | 62.3 | 59.0 | 57.0 | 55.5 | 52.8 | 51.0 | 49.8 | 43.0 | 36.4 | 33.82 | 21.55 | |
| 9 | 60.3 | 57.0 | 55.0 | 53.5 | 51.0 | 49.6 | 48.4 | 42.0 | 36.1 | 33.48 | 21.2 | |
| 10 | 59.8 | 56.0 | 53.7 | 52.1 | 49.6 | 48.2 | 47.1 | 41.0 | 35.5 | 33.14 | 20.85 | |

5.1.1. CALCULATING INVARIANT LATITUDE

Invariant latitude, λ , is found by tracing a magnetic field line from a given point in the equatorial plane to the Earth's surface assuming a centered dipole magnetic field. The geomagnetic latitude (λ_E) of the traced

point is the invariant latitude. Therefore, invariant latitude is (1) equivalent to λ_E for a point already located on the surface of the Earth, and (2) the same for any point along a given magnetic field line. Following *Sauer and Wilkinson* (2008), invariant latitude is expressed as a function of radial distance from the center of the Earth and L-shell

$$r = LR_E \cos^2 \lambda \quad (6)$$

where it is conventional to express r as a function of the Earth's radius (R_E). Therefore, at the surface of the Earth, $r=R_E$, $\lambda=\lambda_E$, and

$$L = \frac{1}{\cos^2 \lambda_E} \quad (7)$$

where the magnetic latitude λ_E is known.

In Figure 1 and Table 2, invariant latitude is calculated at an altitude of 450 km. However, riometer measurements are taken closer to the Earth. *Sauer and Wilkinson* (2008) therefore calculate the poleward shift ($\delta\lambda$) associated with tracing a point along the magnetic field line associated with L at 450 km to a lower altitude of 50 km. Consider the more general case of the poleward shift $\delta\lambda$ associated with a reduction in radius by δr such that $r \rightarrow r - \delta r$ and $\lambda \rightarrow \lambda + \delta\lambda$. Starting with equation (7), $\delta\lambda$ can be solved as follows

$$\begin{aligned} r - \delta r &= LR_E \cos^2(\lambda + \delta\lambda) \\ \frac{r - \delta r}{LR_E} &= (\cos \lambda \cos \delta\lambda - \sin \lambda \sin \delta\lambda)^2 \\ &= \cos^2 \lambda \cos^2 \delta\lambda - 2 \sin \lambda \cos \lambda \sin \delta\lambda \cos \delta\lambda + \sin^2 \lambda \sin^2 \delta\lambda \\ &= \cos^2 \lambda \left(1 - \frac{\delta\lambda^2}{2}\right) - 2 \delta\lambda \sin \lambda \cos \lambda \left(1 - \frac{\delta\lambda^2}{2}\right) + \delta\lambda^2 \sin^2 \lambda \\ &= \delta\lambda^3 [\sin \lambda \cos \lambda] - \delta\lambda^2 \left[\frac{1}{2} \cos^2 \lambda - \sin^2 \lambda\right] - 2 \delta\lambda \sin \lambda \cos \lambda + \cos^2 \lambda \\ &= -2 \delta\lambda \sin \lambda \cos \lambda + \cos^2 \lambda \\ \delta\lambda &= \frac{\delta r}{2R_E \sin \lambda \cos \lambda} \end{aligned}$$

In the above equation, the angle sum and difference trigonometric identities and small angle approximation have been applied. To determine the proton cutoff energy from Table 2 and Figure 1 the invariant latitudes must first be shifted by $\delta\lambda$ using the equation above.

5.1.2. CALCULATING EQUIVALENT KP

In Figure 2, Smart et al. (1999) define K_p in the traditional sense for $K_p < 6$, and use the Boberg extension (Boberg et al., 1995) to define an equivalent K_p using the Dst index for $K_p \geq 6$. The equivalent K_p , K'_p is therefore given by

$$K'_p = \begin{cases} K_p & K_p < 6 \\ \left| \frac{SYM-H}{100} \right| + 6 & K_p \geq 6 \end{cases} \quad (8)$$

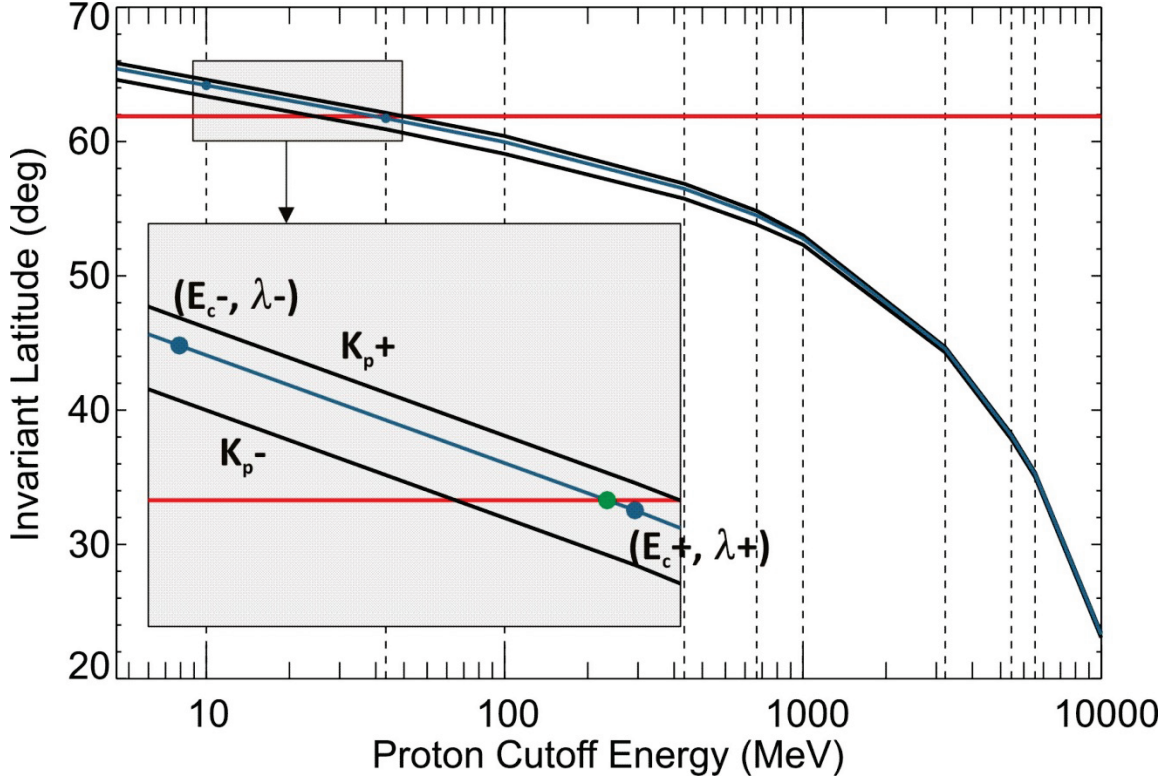


Figure 2: Illustration of how the proton cutoff energy is determined given geomagnetic activity level and magnetic latitude (see description in Section 5.1.3).

where the Dst index used by Smart et al. (1999) has been replaced by the SYM-H index which has a higher time resolution (1-min opposed to 1 hour). Note that because an equivalent K_p index is used for K_p>6, that K_p values >9 are possible. In Smart et al. (1999) a maximum of K_p=10 is allowed.

5.1.3. CALCULATING THE VERTICAL CUTOFF RIGIDITY (E_c)

Once λ and K_p' are known, E_c may be interpolated from the green filled circle in Figure 1. This process is illustrated in detail through an example to explain how the procedure can be programmed. Consider the case where K_p=5+, $\lambda_E=62^\circ$ MLAT, and altitude is 50 km.

The procedure for determining the proton cutoff energy is described as follows, making reference to Figure 2:

1. Determine the equivalent K_p value for the event, as described above. In this case, K_p'=5.33. If K_p were greater than 6, we would be required to calculate the equivalent K_p from the SYM-H index.
2. Find L-shell from equation (7). Here, L=4.54.
3. Using L calculated in step 2, shift the Smart et al. (1999) invariant latitude matrix by $\delta\lambda$.

4. Determine invariant latitude using equation (6) based on the altitude of the measurement (50 km is used for riometer data) and the L shell determined in step 2. Throughout these calculations the Earth's radius is given by $R_E=6371.2$ km. For the example illustrated, $\lambda_E=61.9^\circ$, which is indicated by the horizontal red line in Figure 2.
5. Identify the K_p curves immediately above (K_p+) and immediately below (K_p-) the equivalent K_p . K_p+ and K_p- are indicated by heavy black lines in Figure 2.
6. At each value of E_c in Table 2 (illustrated by vertical dashed lines in Figure 2), linearly interpolate between K_p+ and K_p- to determine the K_p curve for the relevant geomagnetic activity level (see blue curve in Figure 3).
7. Determine where λ_E intersects the K_p curve. Identify the λ and E_c values from Table 2, illustrated in Figure 2, that occur before (E_{c-} , $\delta\lambda_-$) and after (E_{c+} , λ_+) the point of intersection. In Figure 3, blue filled circles are located at coordinates (E_{c+}, λ_+) and (E_{c-}, λ_-) , and the green filled circles indicates the intersection of λ_E with the K_p curve.
8. Calculate the slope and intercept of the line connecting (E_{c+}, λ_+) and $(E_{c-}, \delta\lambda_-)$ and use these values to determine E_c at λ_E , which is the proton cutoff energy.

Once E_c is known, E_o in equation (4) is taken to be the maximum of E_c and 5.2 MeV on the dayside, and the maximum of E_c and 2.2 MeV on the nightside. The maximum of these values is the cutoff energy used to determine the integral proton flux.

5.1.4. CALCULATING INTEGRAL PROTON FLUX

Integral proton is measured at discrete energy levels by the GOES satellites. GOES proton flux data are available for >1 , >5 , >10 , >30 , >50 , >60 , and >100 MeV proton energy cutoffs. The proton energy cutoff E_o calculated for a given time during an event at a given coordinate is unlikely to match one of these discrete values, and interpolation is necessary. Interpolation is performed assuming a power law representation exists between adjacent energy levels. The power law representation is of the form

$$J = J_0 E_0^{-\gamma} \quad (9)$$

where J_0 and γ are constants that must be determined. To do so, first identify the discrete proton cutoff energy level directly above (E_{0+}) and directly below (E_{0-}) the level to be interpolated. Equation (9) may be rearranged to solve for J_0 using both E_{0+} and E_{0-} :

$$J_0 = J_+ E_{0+}^\gamma \quad (10)$$

$$J_0 = J_- E_{0-}^\gamma. \quad (11)$$

Dividing equation (11) by equation (10), γ is found

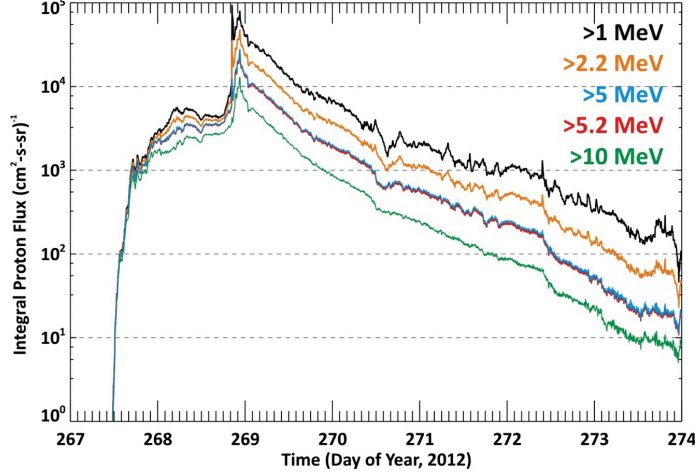


Figure 3: Integral proton flux measured for >1 MeV, >5 MeV, >10 MeV protons and interpolated for >2.2 MeV, >5.2 MeV protons.

$$\gamma = \frac{\ln(J_-/J_+)}{\ln(E_{0+}/E_{0-})} \quad (12)$$

and J_0 is then easily determined from either equation (10) or equation (11). As an example, Figure 3 plots the measured proton flux for >1 MeV (black), >5 MeV (blue), and >10 MeV (green) energetic protons. The orange and red lines show the interpolated flux for >2.2 MeV and >5.2 MeV energy cutoffs, respectively.

Once the procedures outlined in Section 5 are completed for a given instance, absorption may be modelled across the entire high-latitude region. Given the variability of the integral proton flux and K_p , or equivalent K_p , it is recommended that these calculations be independently performed each time new measurements are available.

6. Input data and instrumentation

This section describes data and instruments needed for modeling ionospheric absorption due to polar cap absorption and shortwave fadeout.

6.1. RIOMETERS

Absorption values used for absorption modelling are derived from 30 MHz riometer data collected from a network of riometers located across Canada operated by Natural Resources Canada (NRCan) and the University of Calgary (U of C) (Geospace Observatory Riometer Network (GO-RIO)) (*Rostoker et al.*, 1995; *Danskin et al.*, 2008; *Lam*, 2011). NRCan and GO-RIO data are available at a 1-second resolution and should be filtered prior to consideration to remove noisy and nonphysical data (i.e., see *Fiori and Danskin*, 2017) and to ensure accuracy of the QDC to ensure reliable absorption values. Riometer station locations are indicated in Figure 4 and Table 3.

Table 3: Coordinates of NRCan (three-letter) and GO-RIO (four-letter) riometer stations. Stations are ordered by descending geographic latitude.

| Riometer Station | Geographic Latitude | Geographic Longitude |
|------------------|---------------------|----------------------|
| ALE | 82.52° | 297.73° |
| RES | 74.7° | 265.1° |
| PON | 72.68° | 282.05° |
| CLY | 70.48° | 291.49° |
| TALO | 69.54° | 266.44° |
| CBB | 69.1° | 255.0° |
| HAL | 68.77° | 278.75° |
| INU | 68.3° | 226.5° |
| QIK | 67.55° | 296.0° |
| BLC | 64.3° | 264.0° |
| DAWS | 64.05° | 220.89° |
| IQA | 63.7° | 291.5° |
| RANK | 62.82° | 267.89° |
| YKC | 62.5° | 245.5° |
| FSIM | 61.76° | 238.77° |
| FSMI | 60.03° | 248.07° |
| CHUR | 58.76° | 265.91° |
| RABB | 58.23° | 256.32° |
| MCMU | 56.65° | 248.79° |
| GILL | 56.38° | 265.36° |
| SNK | 56.3° | 281.0° |
| MEA | 54.6° | 246.7° |
| ISLL | 53.86° | 265.34° |
| SAS | 52.2° | 252.88° |
| PINA | 50.20° | 263.96° |
| BRD | 49.92° | 260.05° |
| PEN | 49.32° | 240.37° |
| STJ | 47.6° | 307.3° |
| OTT | 45.4° | 284.5° |

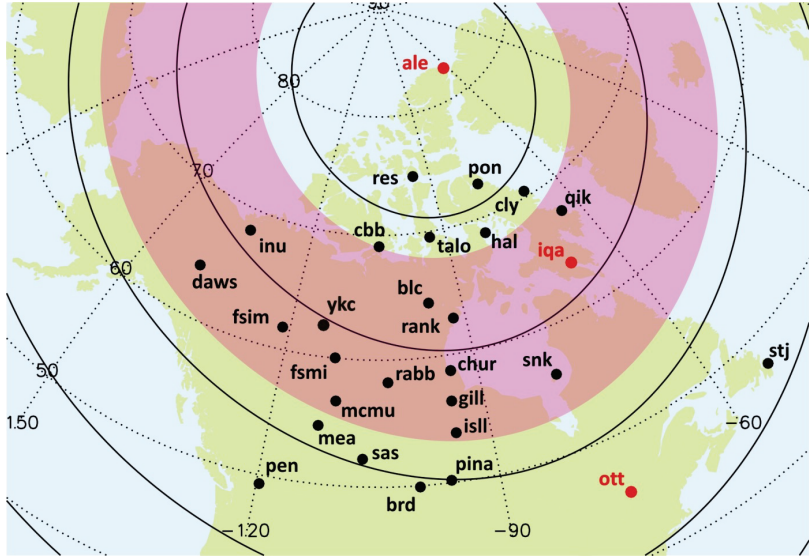


Figure 4: Name and location of NRCAN (three-letter) and GO-RIO (four-letter) riometer stations. Heavy black lines indicate contours for 80°, 70°, 60°, and 50° magnetic latitude. Pink shading between 63° MLAT and 77° MLAT indicates the typical location of the auroral oval.

6.2. GOES SATELLITE DATA

The modelling algorithm described below relies on the relationship between riometer-derived absorption and both the integral proton flux and solar x-ray flux measured by the GOES satellites. Monthly data files are available through SPIDR at <https://satdat.ngdc.noaa.gov/sem/goes/data/avg/> in both 1-min and 5-min formats. Solar proton flux data files contain proton flux data for >1, >5, >10, >30, >50, >60, >100 MeV protons. The >10 MeV proton data are used in this work. Solar X-ray flux data files contain data in the 0.05-0.4 nm and 0.1-0.8 nm range. The 0.1-0.8 nm data are used in this work.

6.3. MAGNETIC INDICES

Calculation of energy cutoffs necessary for determining the integral proton flux require information about geomagnetic activity levels. It is therefore necessary to download the K_p and SYM-H geomagnetic indices. This information is provided, for example, in the 1-minute resolution OMNI_HRO OMNI data files available through the CDAWEB at ftp://cdaweb.gsfc.nasa.gov/pub/data/omni/omni_cdaweb/hro_1min/.

7. Algorithm

The CSWFC absorption modelling algorithm employs the D-RAP modelling technique for modelling absorption due to SWF. For PCA, the algorithm makes use of the optimized D-RAP modelling technique developed by Rogers and Honary (2015) and uses equations and techniques described in Sellers et al. (1977), Sauer and Wilkinson (2008), and Rogers et al. (2016).

The optimized D-RAP approach uses the same equations described above, but treats coefficients m_D and m_N from equation (5) as variable to be determined by minimizing the difference between the measured and modelled absorption.

The algorithm can be summarized in the following steps:

1. **Collect event data.** Collect riometer, solar proton flux, solar x-ray flux, and magnetic data as specified in the previous section.
2. **Optimize the D-RAP model.** In this step, the m_D and m_N slope values from equation (5) which best represents a data set comprised of all available absorption values collected from all available stations over a 30-minute period ending at the time of interest are determined. Optimization is performed at each time step, and data for the time set in question is returned. This is done because for any instance in which m_D and m_N cannot be determined due to an insufficient data set, the previous value of m_D and m_N are assigned to the current value of m_D and m_N . The basic steps for optimization at each time step are as follows:
 - a. Reduce the input absorption array to the 30-minute period ending at the time of interest. If 30-minutes of data does not exist then assign m_D and m_N to default values of $m_D=0.115$ and $m_N=0.020$ (i.e., values determined by *Sellers et al. (1977)* for the Thule riometer). Such a situation only occurs within the first 30-minutes of calculation, or if riometer data is missing from the data file (unlikely).
 - b. Check that there are at least two valid data point poleward of some minimum magnetic latitude cutoff. Absorption data are defined as being valid if the values are finite (non *NaN* and above the noise threshold value of 0.2 dB). The current cutoff latitude is 66° MLAT as current work indicates that absorption at more sub-auroral latitudes are in no way represented by the relationship given in equation (5). Current work also shows the sub-auroral data does not significantly influence the choice of m_D and m_N , mostly because the data is <0.2dB, and that the modelled absorption equatorward of 66° MLAT is wildly inconsistent with measurement-derived values. In the future this threshold may be adjusted. If at least two valid data points exist, and if at least two valid data points come from the region poleward of the auroral oval, then continue. Otherwise, m_D and m_N are assigned the previous values of m_D and m_N .
 - c. Once valid data points are identified, m_D and m_N are determined using standard singular value decomposition (SVD) techniques to minimize the difference between the measurement-derived and modelled absorption. m_D can be solved if there are at least two dayside points ($\epsilon'=10^\circ$) in the valid data set. m_N can be solved if there are at least two nightside points ($\epsilon'=-10^\circ$) in the valid data set. Twilight data ($-10^\circ < \epsilon' < 10^\circ$) can be used toward the solution only if there are at least two dayside AND two nightside points.
3. **Calculate absorption due to PCA.** Using the values of m_D and m_N determined in the previous step, calculate absorption across the entire high-latitude region using equation (5).

4. **Calculate absorption due to SWF.** If the solar X-ray flux is $> 1.0 \times 10^{-5} \text{ Wm}^2$ then model the absorption across the entire high-latitude region using equations (2) and (3).

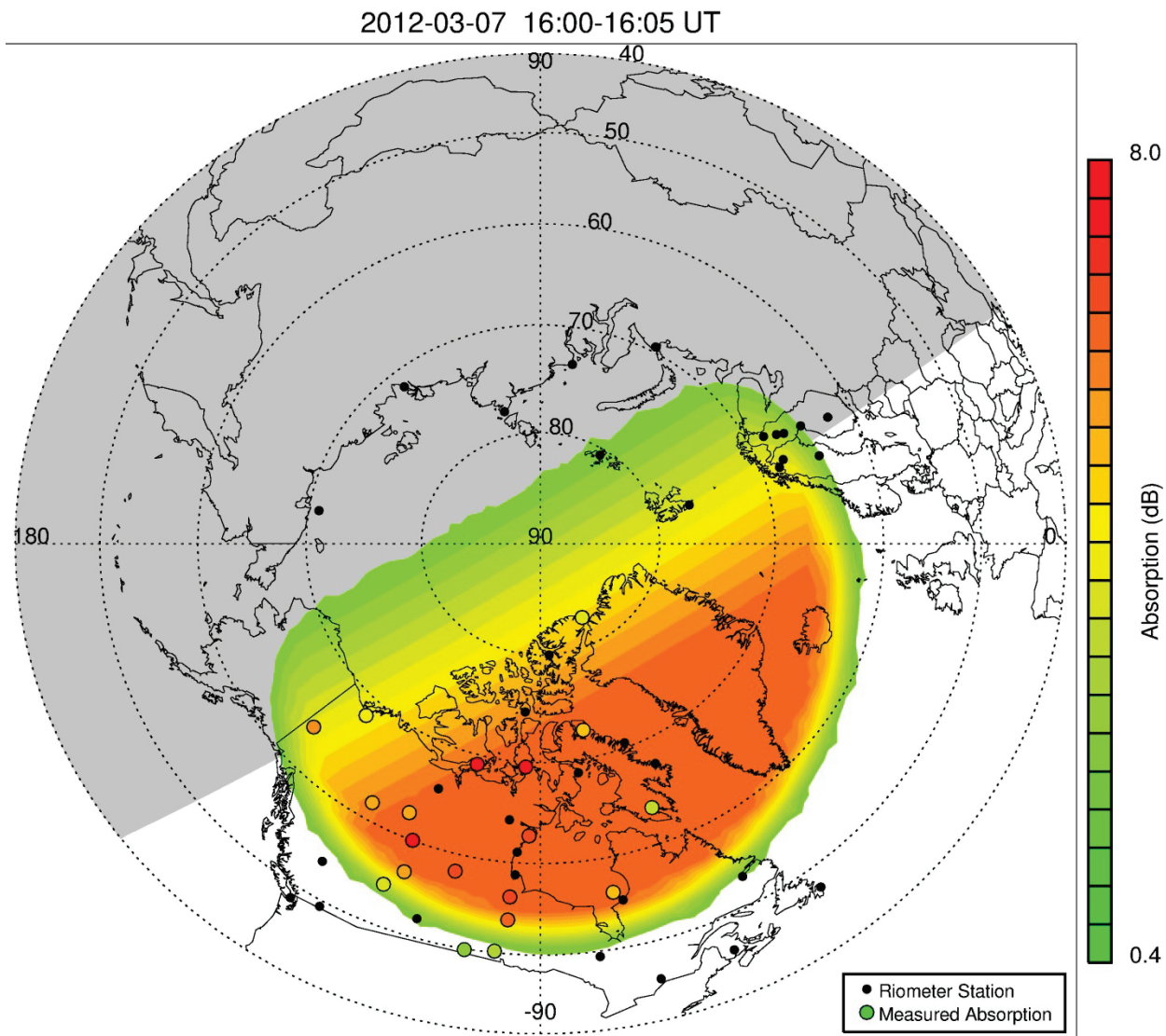
Figure 5 shows an example of the absorption modelled using the CSWFC absorption modelling algorithm. Modelled absorption is represented using colored contours and measurement-derived absorption is indicated by filled circles at the measurement coordinates. The lower limit of the plotted absorption is 0.4 dB; values < 0.4 dB are considered to be noise. The colour bar ranges from green to red and is meant to provide a traffic light style representation of absorption values where green indicates good HF radio propagation conditions ('go') and red indicates poor conditions ('stop'). A statistical study of typical absorption levels and transmission quality is required to accurately set the upper limit of the colour bar.

Although the example plot shown in Figure 5 is pleasing to the eye, there are obvious discrepancies between the measurement-derived and modelled absorption. Differences range from < 3 dB at low latitudes (Pinawa and Brandon) to as much as 12 dB at Fort Smith.

The differences between measured and modelled absorption, as illustrated by Figure 5 is hardly representative. Map accuracy varies quite widely. For example, consider maps presented in Figure 6 and Figure 7.

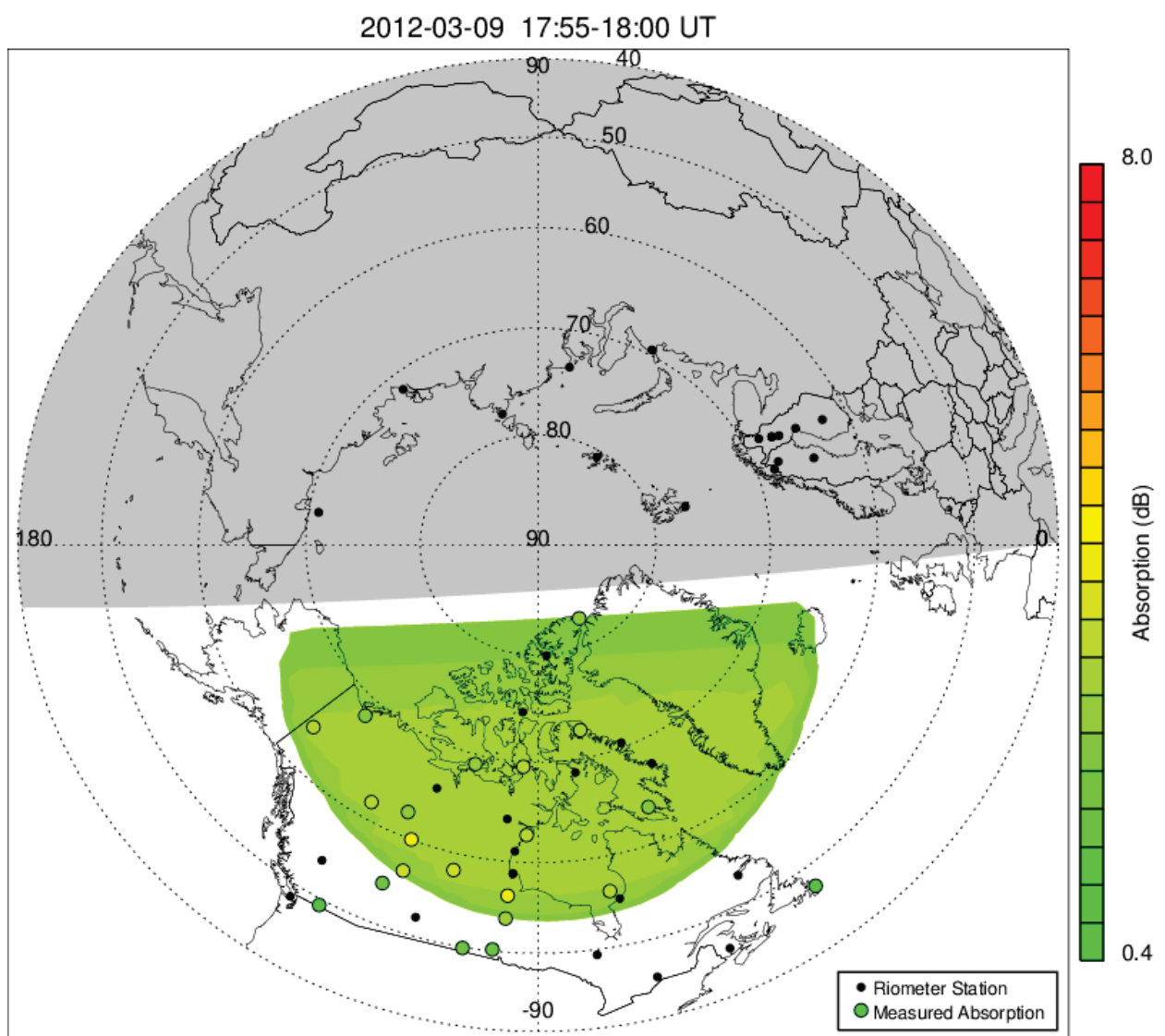
In Figure 6, absorption is plotted for a relatively quiet period with measurement-derived absorption values peaking at 4.14 dB. Here the modelled absorption closely matches measurements, but the maximum difference still reaches 2 dB. Figure 7 represents a worst case scenario. Despite the overall smooth appearance of the modelled absorption, measurements are severely underestimated with differences ranging from 2.6 to 18.2 dB, and an average difference of 5.6 dB.

From these examples it is clear that neither the D-RAP model, nor the optimized D-RAP model is able to completely represent measured absorption. The exact cause of this is unclear. It is possible that the absorption model smooths out local absorption features. It is also possible that the absorption model, which was originally derived based on data from a single high-latitude station, is not transferrable to lower latitudes. Investigation of the source of the discrepancy is left for future work.



Canada

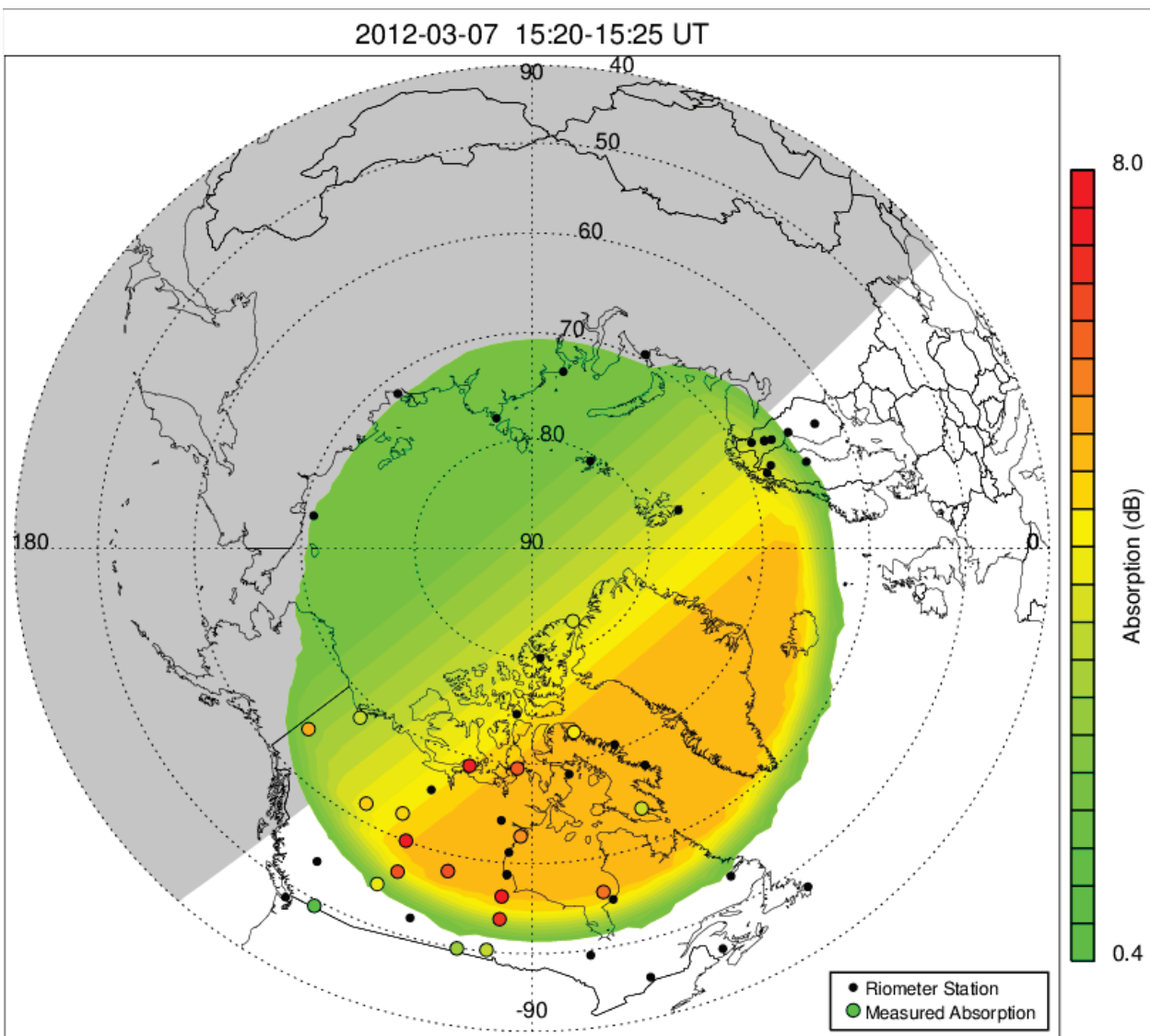
Figure 5: Absorption modelled using the NRCan absorption modelling algorithm. Black filled stations indicate the location of NRCan, NORSTAR, AARI, SGO, and IRF riometers. Absorption magnitude is defined by the colour bar. Coloured filled circles at riometer stations locations indicated the absorption derived from riometer measured. Grey shading indicated the location of the nightside determined at the ground. The time period represented by the plot is indicated at the top of the Figure and the time the plot was generated is indicated at the lower left.



Generated at: 2016-03-02 15:53 UT

Canada

Figure 6: Same as Figure 5, for a different interval.



Generated at: 2016-03-02 15:58 UT

Canada 

Figure 7: Same as Figure 5, for a different interval.

8. Summary

This report describes, in detail, the algorithm currently applied by the Canadian Space Weather Forecaster Center for modelling ionospheric absorption due to polar cap absorption (PCA) and shortwave fadeout (SWF) based on the D-region absorption prediction (D-RAP) model, with improvements reported in the literature (Rogers and Honary, 2015; Rogers et al, 2016).

Minor differences (<1 dB) between measured and modelled values are expected for any modelling technique but larger differences can have severe implications for users. Discrepancies between the measurement-derived and model absorption can be attributed to several factors. Deficiencies exist in the underlying D-RAP model itself. Papers or reports which thoroughly examines the performance of the D-RAP model were not found. It is likely that such studies have been performed internally without being published. There is one validation report written by the D-RAP validation team which states “*the [D-RAP] model output should be treated as a qualitative indicator of highly perturbed conditions*” rather than as a definitive model of the expected absorption (Akmaev et al., 2010). The validation team also recommends that the *Sauer and Wilkinson* (2008) PCA model requires improvement. In addition to deficiencies in the underlying model, there can be inconsistencies in the riometer data itself due to differences between the calibration of instruments operated by different centers, or local phenomenon. Finally, the model only accounts for two forms of absorption and would greatly improve through the addition of models for absorption due to other sources such as auroral absorption and sudden commencement absorption.

9. References

- Akmaev, R. A. for the Validation Team (A. Newman, M. Codrescu, C. Schulz, E. Nerney) (2010), D-RAP model validation: I. Scientific Report. Available from <https://www.ngdc.noaa.gov/stp/drap/DRAP-V-Report1.pdf>.
- Boberg, P. R., A. Tylka, J. Adams, E. O. Flückiger, E. Kobel (1995), Geomagnetic transmission of solar energetic particles during the geomagnetic disturbance of October 1989, *Geophys. Res. Lett.*, 22, 1133-1136. Available from <https://doi.org/10.1029/95GL00948>.
- Browne, S., J. K. Hargreaves, and B. Honary (1995), An imaging riometer for ionospheric studies, *Electron. Commun. Eng. J.*, 7 (5), pp. 209-217, <http://dx.doi.org/10.1049/ecej:19950505>.
- Cannon, P., M. Angling, L. Barclay; C. Curry, C. Dyer, R. Edwards, G. Greene, M. Hapgood, R. Horne, D. Jackson, C. Mitchell, J. Owen, A. Richards, C. Rogers, K. Ryden, S. Saunders, M. Sweeting, R. Tanner, A. Thomson, and C. Underwood (2013), Extreme space weather: impacts on engineered systems and infrastructure. London, Royal Academy of Engineering. Available from <https://www.raeng.org.uk/publications/reports/space-weather-full-report..>
- Danskin, D. W., D. Boteler, E. Donovan, E. Spanswick (2008), The Canadian riometer array, Proc. of the 12th International Ionospheric Effects Symposium, IES 2008.
- Davies, K. (1990), Ionopsheric Radio, IEE Electromagn. Ser. Peter Peregrinus, London, vol. 31, pp. 580.
- Fiori, R. A. D., D. W. Danskin (2016), Examination of the relationship between riometer-derived absorption and the integral proton flux in the context of modeling polar cap absorption, *Space Weather*, 14, 1032-1052, <https://doi.org/10.1002/2016SW001461>.
- Foppiano, A. J., and P. A. Bradley (1984), Day-to-day variability of riometer absorption, *J. Atmos. Terr. Phys.*, 46 (8), pp. 689-696, [https://doi.org/10.1016/0021-9169\(84\)90130-2](https://doi.org/10.1016/0021-9169(84)90130-2).
- Frissell, N. A., E. S. Miller, S. R. Kaepller, F. Ceglia, D. Pascoe, N. Sinanis, P. Smith, R. Williams, and A. Shovkoplyas (2014), Ionospheric sounding using real-time amateur radio reporting networks, *Space Weather*, 12, pp. 651-656, <https://doi.org/10.1002/2014SW001132>.
- Frissell, N. A., J. S. Vega, E. Markowitz, A. J. Gerrard, W. D. Engelke, P. J. Erickson, E. S. Miller, R. C. Luetzelschwab, J. Bortnik (2019), High-frequency communications response to solar activity in September 2017 as observed by amateur radio networks, *Space Weather*, 17(1), pp 118-132, <https://doi.org/10.1029/2018SW002008>.
- Gopalswamy, N. (2003), Coronal mass ejections: initiation and detection, *Adv. Space Res.*, 31 (4), 869-881, [https://doi.org/10.1016/S0273-1177\(02\)00888-8](https://doi.org/10.1016/S0273-1177(02)00888-8).
- Hargreaves, J. K. (1992), The Solar-Terrestrial Environment, Cambridge University Press, Cambridge, UK.
- Hosokawa K., T. Iyemori, A. S. Yukimatu, and N. Sato (2000), Characteristics of solar flare effect in the high-latitude ionosphere as observed by the SuperDARN radars, *Ad. Polar Upper Atmos. Res.*, 14, pp. 66-75.

Hargreaves, J. K., A. V. Shirochkov, and A. D. Farmer (1993), The polar cap absorption event of 19-21 March 1990: recombination coefficients, the twilight transition and the midday recovery, *J. Atmos. Terr. Phys.*, 55 (6), 857-862, [https://doi.org/10.1016/0021-9169\(93\)90026-U](https://doi.org/10.1016/0021-9169(93)90026-U).

Hargreaves, J. K. (2010), Auroral radio absorption: The prediction question, *Adv. Space Res.*, 45, pp. 1075–1092, <https://doi.org/10.1016/j.asr.2009.10.026>.

Hunsucker, R. D. (1992), Auroral and polar-cap ionospheric effects on radio propagation, *IEEE transactions on antennas and propagation*, 40 (7), 818-828, <https://doi.org/10.1109/8.155747>.

Hunsucker, R. D., and J. K. Hargreaves (2003), The high-latitude ionosphere and its effects on radio propagation, *Cambridge atmospheric and space science series*, Cambridge University Press, Cambridge.

Kavanagh, A. J., S. R. Marple, F. Honary, I. W. McCrea, and A. Senior (2004), On solar protons and polar cap absorption: constraints on an empirical relationship, *Ann. Geophys.*, 22(4), pp. 1133-1147, <https://doi.org/10.5194/angeo-22-1133-2004>.

Kouznetsov, A., D. J. Knudsen, E. F. Donovan, and E. Spanswick (2014), Dynamics of the correlation between polar cap radio absorption and solar energetic proton fluxes in the interplanetary medium, *J. Geophys. Res.*, 119, 1627-1642, <https://doi.org/10.1002/2013JA019024>.

Lam, H.-L. (2011), From early exploration to space weather forecasts: Canada's geomagnetic odyssey, *Space Weather*, 9, S05004, <https://doi.org/10.1029/2011SW000664>.

Little, C. G., and H. Leinbach (1959), The riometer – a device for the continuous measurement of ionospheric absorption, *Proceedings of the IRE*, 315-320.

MacAlester, M. H., and W. Murtagh (2014), Extreme space weather impact: An emergency management perspective, *Space Weather*, 12, 530-537, <https://doi.org/10.1002/2014SW001095>.

Neal, J. J., C. J. Rodger, and J. C. Green (2013), Empirical determination of solar proton access to the atmosphere: Impact on polar flight paths, *Space Weather*, 11, 420-433, <https://doi.org/10.1002/swe.20066>.

National Research Council (2008), Severe space weather events – Understanding societal and economic impacts: a workshop report, Natl. Acad. Press, Washington, D.C., pp 144. Available from <http://lasp.colorado.edu/home/wp-content/uploads/2011/07/lowres-Severe-Space-Weather-FINAL.pdf>.

Pirjola, R., K. Kauristie, H. Lappalainen, A. Viljanen, and A. Pulkkinen (2005), Space weather risk, *Space Weather*, 3 (S02A02), <https://doi.org/10.1029/2004SW000112>.

Rodger, C., M. A. Clilverd, P. T. Verronen, T. Ulich, M. J. Jarvis, and E. Turunen (2006), Dynamic geomagnetic rigidity cutoff variations during a solar proton event, *J. Geophys. Res.*, 111, A04222, <https://doi.org/10.1029/2005JA011395>.

Rogers, N. C., and F. Honary (2015), Assimilation of real-time riometer measurements into models of 30 MHz polar cap absorption, *Journal of Space Weather and Space Climate*, 5, pp. 1-18., <https://doi.org/10.1051/swsc/2015009>.

Rogers, N. C., A. Kero, F. Honary, P. T. Verronen, and E. M. Warrington (2016), Improving the twilight model for polar cap absorption nowcasts, *Space Weather*, 14, 950-972, <https://doi.org/10.1002/2016SW001527>.

Rostoker, G., J. C. Samson, F. Creutzberg, T. J. Hughes, D. R. McDiarmid, A. G. McNamara, A. Vallance Jones, D. D. Wallis, and L. L. Cogger (1995), CANOPUS – A ground-based instrument array for remote sensing the high latitude ionosphere during the ISTP/GGS program, *Space Science Reviews*, 71(1), 743-760.

Sauer, H., and D. C. Wilkinson (2008), Global mapping of ionospheric HF/VHF radio wave absorption due to solar energetic protons, *Space Weather*, 6, S12002, <https://doi.org/10.1029/2008SW000399>.

Schumer, E. A. (2009), Improved modeling of midlatitude D-region ionospheric absorption of high frequency radio signals during solar x-ray flares. Ph.D. dissertation, AFIT/DS/ENP/09-J01, United States Air Force, Wright-Patterson Air Force Base, Ohio, USA, p. 49, June 2009.

Sellers, B., and F. A. Hanser (1977), The night and day relationships between polar cap riometer absorption and solar protons, *Radio Science*, 12(5), pp. 779-789, <https://doi.org/10.1029/RS012i005p00779>.

Smart, D. F., M. A. Shea, E. O. Fluckiger, A. J. Tylka, P. R. Boberg (1999), Changes in calculated vertical cutoff rigidities at the altitude of the international space station as a function of geomagnetic activity Proc. Int. Cosmic Ray Conf., 7, 337-340.

Smart, D. F., M. A. Shea, A. J. Tylka, and P. R. Boberg (2006), A geomagnetic cutoff rigidity interpolation tool: Accuracy verification and application to space weather, *Advances in Space Research*, 37, 1206-1217, <https://doi.org/10.1016/j.asr.2006.02.011>.

Stonehocker, G. H. (1970), Advanced telecommunication forecasting technique in AGY, 5th, Ionospheric forecasting, AGARD Conf. Proc., 29, 27-31.